Intertwined eco-morphodynamic evolution of salt marshes and tidal channels cutting through them

Liang Geng[1,2], Andrea D'Alpaos[3], Alessandro Sgarabotto[2], Zheng Gong[1], and Stefano Lanzoni[2]

[1]State Key Laboratory of Hydrology Water Resources and Hydraulic Engineering, Hohai University, Nanjing, China
[2]Department of Civil, Environmental and Architectural Engineering, University of Padova
[3]Department of Geosciences, University of Padova

Key Points:

- Vegetation with lower optimal elevation strongly promotes the development, complexity and drainage efficiency of channel networks.
- Vegetation patches affect the distribution of sediment deposition by trapping sediment and reducing the landward sediment transport.
- Sea level rise restricts the extension of salt marshes and consequently leads to reduced control of vegetation on tidal channel development.

Corresponding author: Liang Geng, liang.geng@dicea.unipd.it

Abstract

The formation and development of tidal channels and salt marshes are controlled by complex interactions between hydrodynamics, sediment transport, and vegetation dynamics. Tidal channels affect and, at the same time, are affected by the growth of salt marshes fringing them. The coupled evolution of these morphological units is thus a key ingredient for simulating the typical behaviour of tidal environments. We developed a mathematical model accounting for vegetation-induced flow resistance and wetting-drying processes typical of tidal environments, to investigate the eco-morphodynamic evolution of intertidal areas fringing a main channel and of the tidal creeks cutting through them. Model results indicate that vegetation promotes the development of channel networks, leading to more complex channel structures and higher drainage efficiency. Vegetation encroachment influences sediment deposition patterns by trapping sediment in the seaward and middle intertidal areas, while reducing the amount of sediment delivered to landward areas. In the presence of sea level rise, this deficit of sediment enhances the landward-decreasing trend of the intertidal platform and leads to more isolated vegetation patches. Overall, sea level rise restricts the extension of salt marshes and consequently reduces the effect of vegetation on channel development.

Plain Language Summary

Tidal channels in coastal landscapes connect the sea and the landward salt marshes, acting as essential drainage pathways for exchanging water, sediments, and nutrients. The effect of vegetation on channel morphology strongly influence the morphodynamic evolution of the intertidal zone. In this study, a tide-dominated intertidal basin is simulated through a numerical model to analyze the mutual relations between vegetation growth and channel development. Vegetation better suited to live at lower elevations strongly promotes channel development, creating a more efficient drainage system. As the seaward vegetation patches trap the sediment coming from the sea, less sediment is transported to the landward areas, leading to a lower landward deposition rate. Furthermore, sea-level rise restricts vegetation growth and thus reduces the effects of vegetation on tidal channel development.

1 Introduction

Tidal flats and salt marshes connect the land and the ocean by mediating the exchange of water, sediments and nutrients within coastal landscapes (Mitsch & Gosselink, 2000; Zedler & Kercher, 2005; FitzGerald & Hughes, 2019). Salt marshes are typically covered by halophytic vegetation. They occupy elevations higher than mean sea level (MSL) and are periodically inundated by the tide (Allen, 2000; Friedrichs & Perry, 2001). Conversely, tidal flats lie below mean sea level and, hence, are intermittently exposed during low tides (Zhou et al., 2016). They do not host halophytic vegetation, but can be covered by microbial biofilms or colonized by sea grasses which contribute to stabilize the sediment bed (Yallop et al., 1994; Chen et al., 2017).

Depending on the rate of relative sea level rise (RSLR) and sediment availability, tidal flats can evolve into salt marshes and vice versa (Fagherazzi et al., 2006; Marani et al., 2007; Zhou et al., 2016). As the elevation of the intertidal platform increases within the tidal frame, flow conditions become suitable for the settlement of vegetation seeds. The bare surface of tidal flats is thus progressively encroached by vegetation patches, and eventually a salt marsh forms as a result of the interaction of physical and biological processes (Bouma et al., 2014; Hu et al., 2015). On the contrary, a salt marsh can experience a transition into a tidal flat when marsh accretion rate is lower than the rate of RSLR, and the marsh platform progressively drowns (Kirwan et al., 2010; D'Alpaos et al., 2011). The window of opportunity (Balke et al., 2011, 2014; Hu et al., 2015) for vegetation growth

is reduced and vegetation progressively disappears (Morris et al., 2002; Kirwan & Megonigal, 2013). Salt marshes can also undergo a transition into tidal flats through lateral retreat of marsh edges. These edges are characterized by scarps between the vegetated marsh surface and the bare tidal flat bottom facing the marsh. Wind waves impinge against salt marsh edges, leading to marsh lateral retreat, and erode sediments from the tidal flats, promoting their deepening (e.g. Marani et al., 2011; Mariotti & Fagherazzi, 2013; Leonardi & Fagherazzi, 2014; Leonardi et al., 2016). Deeper and wider tidal flats favor the development of stronger wind waves (Mariotti & Fagherazzi, 2013; Tommasini et al., 2019) and, consequently, enhance wave-induced erosion of the salt marsh border (Bendoni et al., 2016).

The evolution of tidal flats and salt marshes is strongly related to tidal channel dynamics. Both tidal channel and intertidal platform evolution are governed by the interactions between hydrodynamics, sediment transport, morphological changes, and biological effects (D'Alpaos et al., 2007; Temmerman et al., 2007; De Swart & Zimmerman, 2009; Vandenbruwaene et al., 2011; Gong et al., 2018; Zhao et al., 2019; Li et al., 2019). The mutual feedbacks (either positive or negative), which characterize these interactions, control the so-called *Morphodynamic Loop* (Wright & Thom, 1977; Cowell & Thom, 1994; Coco et al., 2013). Given proper initial and boundary conditions, the overall evolution of tidal systems is controlled by the interplay between the various morphological units (tidal channels, tidal flats and salt marshes). Tidal channels act as preferential drainage pathways (D'Alpaos et al., 2005; Hughes, 2012; Coco et al., 2013; Zhou et al., 2014) and, hence, regulate sediment distribution within the tidal system. In addition, sediment availability determines the fate of tidal flats and salt marshes in response to increasing sea levels and wave-induced lateral erosion (Mariotti & Fagherazzi, 2013). In turn, intertidal platform elevation within the tidal frame controls the tidal prism, ultimately determining the size and extent of tidal channel networks (e.g. D'Alpaos et al., 2006; van der Wegen et al., 2010; Stefanon et al., 2012; Kleinhans et al., 2015).

Vegetation dampens tidal flow energy and strengthens the soil through the roots. Vegetation thus reduces erosional processes and enhances sediment deposition through trapping and organic soil production (Toy et al., 2002; Temmerman et al., 2005; Mudd et al., 2010; D'Alpaos & Marani, 2016). In the early stages of salt marsh formation, the flow concentration favored by pioneering vegetation patches causes erosion and channel initiation (Temmerman et al., 2007; Vandenbruwaene et al., 2011; Temmerman et al., 2012; Van Oyen et al., 2014). On the surface of fully-colonized salt marshes, the increased flow resistance leads to flux concentration within channels, enhancing their initiation and further incision (Temmerman et al., 2007). However, the reduction experienced by the tidal prism as marsh elevation increases leads to weaker in-channel currents and counteracts channel scouring (D'Alpaos et al., 2006). The elevation of the intertidal platform in the tidal frame, in turn, dictated by sediment availability and the rate of RSLR, controls which effect prevails over the other (Sgarabotto et al., 2021). In general, the width-to-depth ratio of salt marsh channels is smaller than that of channels cutting through tidal flats (Marani et al., 2002; Fagherazzi et al., 2004; Lawrence et al., 2004; D'Alpaos et al., 2005; Vandenbruwaene et al., 2012; Sgarabotto et al., 2021).

RSLR adds a further degree of complexity. The growth of halophytic vegetation depends on bed elevation within the tidal frame (Morris et al., 2002; Mudd et al., 2004). Long periods of submergence are unsuitable for the survival of halophytic plants because of the poor soil aeration. Therefore, high rates of RSLR threaten the survival of salt marshes (Marani et al., 2007; Kirwan & Temmerman, 2009; Coco et al., 2013) and can prevent their development. These morphological units can thus keep pace with the increasing sea levels only if sediment supply and organic soil production by vegetation are high enough to counterbalance the effects of RSLR (Pilkey & Cooper, 2004; Kirwan et al., 2010; D'Alpaos et al., 2011; Lovelock et al., 2011).

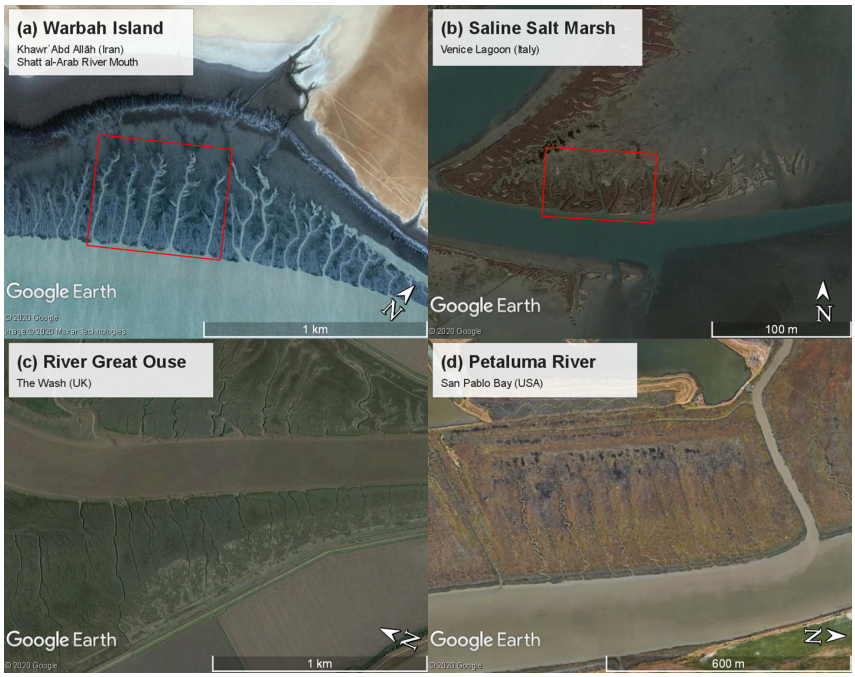

Figure 1. Typical examples of intertidal areas flanking a main tidal channel/river: a) Bare tidal flats on Warbah Island, N29^{o}57'20"-E48^{o}02'05" (Kuwait); b) Salt marsh along the Dell'Ancora Channel, N45^{o}31'06"-E12^{o}28'52" (Venice Lagoon, Italy); c) Salt marsh at the mouth of River Great Ouse, N52^{o}48'04"-E00^{o}21'23" (United Kingdom); d) Salt marsh along the Petaluma River, N38^{o}07'39"-W122^{o}30'42" (California, USA). Source: Google Earth.

Only a few studies simulate the intertwined eco-morphodynamic evolution of salt marshes and tidal channels cutting through them (D'Alpaos et al., 2007; Temmerman et al., 2007; Belliard et al., 2015; Mariotti, 2018; Sgarabotto et al., 2021), accounting for the mutual interactions among these morphological units. In this contribution, we unravel the relative importance of biogeomorphic feedbacks through the analysis of the evolution of a tidal environment composed by narrow intertidal areas flanking large tidal channels or tidal rivers. Some examples of this type of tidal environments are shown in Figure 1. Typically, a series of almost evenly spaced channels, directed perpendicularly to the main channel, feed and drain the considered intertidal area, consisting either of bare tidal flats (Figure 1a) or salt marshes (Figures 1b-d).

Starting from an initially flat intertidal platform, we simulate the evolution of the system under the action of prescribed tidal forcing, sediment input and sea level rise. Vegetation is assumed to encroach the platform as a reference threshold elevation is exceeded. Vegetation patches then develop in a dynamic bed topography characterized by extending tidal channels. Vegetation feedbacks on tidal channel structure are elucidated by comparing the morphologies computed in the presence of vegetation with those obtained considering the evolution of bare tidal flats subjected to the same forcings.

The rest of the paper is structured as follows. Section 2 describes the model developed for the analysis of the eco-morphodynamic evolution of the considered systems and the design of the numerical simulations. Section 3 reports the numerical results in terms of bed topographies, spatial distributions of vegetation biomass, mean erosion/deposition rates, and tidal channel features. These results are discussed in Section 4 with specific

attention to the effects of RSLR, the comparison with field data, and the limitations intrinsic to the modeling approach. Finally, Section 5 is devoted to the conclusions.

2 Material and Methods

2.1 Model Setup

The proposed eco-geomorphic model includes four modules to simulate the interactions among the three main morphological units (tidal channels, tidal flats, and salt marshes) which generally compose a tidal basin. The different modules deal with tidal currents, sediment transport, bed evolution, and vegetation growth. Before describing in detail these modules, it is worth briefly describing how the modules are related to each other.

Essentially, we assume that hydrodynamics and bed evolution are characterized by different temporal scales. In other words, the flow field is taken to adapt almost instantaneously to changes in bed elevation. These latter changes, in fact, are supposed to be relatively smooth in space and to need several tidal cycles for exerting their feedback on the flow field. At each time step of a characteristic tidal cycle, stemming from the prescribed tidal forcing, the spatial distribution of flow velocity is used to solve the advection-dispersion equation for the suspended sediment concentration. At the same time, cumulative erosion/deposition rates are computed at each bed location based on the spatial distribution of bed shear stresses exerted by the flow. In the presence of vegetation, trapping of sediment and organic soil production are accounted for in the computation of deposition, while erosion is taken to be negligible. Vegetation biomass, which is computed as a function of bed elevation, modifies the friction term in the hydraulic module. At the end of any characteristic tidal cycle, the bed elevation is updated by employing the tidally averaged erosion/deposition rates multiplied by a morphological factor. The characteristic tidal cycle is then repeated.

2.1.1 Hydraulic module

We consider an intertidal basin dominated by tidal forcing. As a first approximation, wind action and possible river inflows are not considered. The flow field is described through a suitably simplified version of the two-dimensional (2D) depth-averaged momentum and mass conservation equations developed by Defina (2000) to account for wetting and drying processes. At each instant t of the tidal cycle, the free surface elevation h is assumed to be given by the sum of a constant contribution ξ, coinciding with the water elevation prescribed at the seaward boundary, and a variable contribution, ζ, which expresses the local variation of the free surface with respect to the average water level (Figure 2), namely:

$$h(x, y, t) = \xi(t) + \zeta(x, y, t), \tag{1}$$

where x is the landward directed cartesian coordinate, with origin at the seaward boundary and y is the transverse cartesian coordinate. Both the quantities h and ζ are referred to MSL.

Owing to the relatively small flow depths typical of the investigated flows, friction is assumed to prevail over inertia and, consequently, to balance the free surface slope in the momentum equations (Rinaldo et al., 1999; D'Alpaos et al., 2007). By evaluating the bed shear stress through the Gauckler-Strickler resistance law, it is easily demonstrated that the mass and momentum conservation equations take the form

$$\psi \frac{\partial h}{\partial t} + \frac{\partial (D\,U_x)}{\partial x} + \frac{\partial (D\,U_y)}{\partial y} = 0, \tag{2}$$

$$\frac{\partial h}{\partial x} = -\frac{U_x \sqrt{U_x^2 + U_y^2}}{K_s^2} \left(\frac{D}{\phi}\right)^2, \tag{3}$$

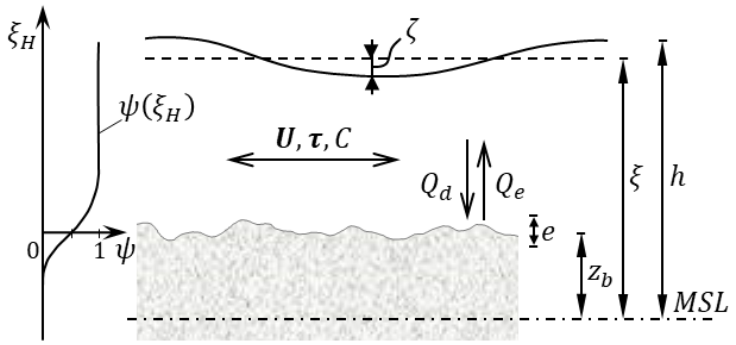

Figure 2. Sketch of the flow field and relevant notations.

$$\frac{\partial h}{\partial y} = -\frac{U_y \sqrt{U_x^2 + U_y^2}}{K_s^2} \left(\frac{D}{\phi}\right)^2, \tag{4}$$

with

$$D = \frac{e}{4}\left[\frac{1}{\sqrt{\pi}} \exp\left(-\xi_H^2\right) - \xi_H \, erfc\left(\xi_H\right)\right], \tag{5}$$

$$\psi = \frac{1}{2} erfc\left(\xi_H\right), \tag{6}$$

$$\phi = \left[D + 0.27\sqrt{e\,D}\,\exp(-2\,D/e)\right]^{5/3}. \tag{7}$$

Here, U_x and U_y are the longitudinal and transverse components of the depth-averaged velocity, respectively; D is the effective water depth; K_s is the Gauckler-Strickler resistance coefficient; ψ and ϕ are two functions (the first dimensionless) arising from the depth-averaging of the relevant equations over a representative elementary area to account for wetting and drying effects (Defina, 2000), and *erfc* is the complementary error function. The quantities D, ψ, and ϕ depend on the dimensionless variable

$$\xi_H = -2\,\frac{h - z_b}{e}, \tag{8}$$

where z_b is the bed elevation referred to MSL and e is a characteristic scale of variations of bed elevation over the representative elementary area (i.e. a subgrid averaged roughness).

Note that the method chosen here to deal with wetting/drying processes allows one to always solve the same set of equations, without the need of removing/adding elements as the domain gets wet/dry. If the water level is much higher than the bed level, the effective water depth becomes equal to the local flow depth $h - z_b$. Conversely, if $h - z_b$ is very small (even negative if the bed gets dry), D approaches a very small positive value that simulates a partially-wet condition.

Recalling the definition of the free surface elevation (1), the simplified momentum equations (3) and (4) can be rewritten in the form

$$U_x = -\frac{K_s^2}{\sqrt{U_x^2 + U_y^2}} \left(\frac{\phi}{D}\right)^2 \frac{\partial \zeta}{\partial x}, \tag{9}$$

$$U_y = -\frac{K_s^2}{\sqrt{U_x^2 + U_y^2}} \left(\frac{\phi}{D}\right)^2 \frac{\partial \zeta}{\partial y}. \tag{10}$$

Substituting these expressions into (2), and setting $U = \sqrt{U_x^2 + U_y^2}$, we obtain the following equation (Van Oyen et al., 2014)

$$\psi \left(\frac{d\xi}{dt} + \frac{\partial \zeta}{\partial t} \right) - \left[\frac{\partial}{\partial x} \left(\frac{K_s^2 \, \phi^2}{U \, D} \frac{\partial \zeta}{\partial x} \right) + \frac{\partial}{\partial y} \left(\frac{K_s^2 \, \phi^2}{U \, D} \frac{\partial \zeta}{\partial y} \right) \right] = 0, \tag{11}$$

that describes the spatio-temporal variation of the water level $\zeta(x, y, t)$ given the water elevation at the seaward boundary ξ.

Equation (11) is solved numerically through finite differences. The spatial derivatives are discretized through central differences, while forward differences are employed for the temporal derivative $\partial\zeta/\partial t$. The resulting system of equations is solved with the open-source computational package "Pardiso". At each time step, Picard iteration is used to deal with the nonlinear terms involving U. At the first iteration, U is set equal to the magnitude of the velocity at the previous time step. After solving for ζ, at the next iteration, U is updated based on the values of U_x and U_y given by equations (9) and (10), respectively. The iteration stops when the percentage difference between the values of ζ computed at previous and current iterations is less than a prescribed small value (5 %).

The boundary conditions associated with the system of partial differential equations (9), (10), and (11) consist of the water level at the sea boundary, where ξ is taken equal to a cosine tidal wave with amplitude a_0, while no-flux conditions are imposed at the other boundaries of the simulated tidal basin. The geometry of this domain is described below, in the paragraph concerning the design of numerical experiments.

At the initial instant of any simulation, a constant water level is prescribed throughout the basin at high water slack, equal to the high tide level, while the flow velocity is set everywhere to zero. The simulation thus starts with the ebb phase.

2.1.2 Sediment transport

Sediments are assumed to be transported mainly as suspended load, owing to their fine size. Their dynamics is described by the two-dimensional advection-dispersion equation (e.g. D'Alpaos et al., 2007)

$$\frac{\partial (C \, D)}{\partial t} + \nabla (C \, D \, \boldsymbol{U} - k_m \, D \, \nabla C) = Q_e - Q_d, \tag{12}$$

where C is the depth-averaged suspended sediment concentration, $\boldsymbol{U}$ is the depth-averaged velocity vector, k_m is the horizontal mixing coefficient, and Q_e and Q_d are the rate of erosion and deposition, respectively. Equation (12) is solved numerically by an explicit central difference method.

During the flood phase, a given external suspended sediment concentration C_{sea} is imposed at the seaward boundary of the tidal basin. Conversely, during the ebb phase sediments are transported out of the tidal basin. The suspended sediment concentration at the seaside boundary is thus determined by the sediment concentration coming from upstream. According to these boundary conditions, the suspended sediment is conveyed into the tidal basin and redistributed therein by the flood currents. Conversely, ebb currents usually tend to flush out the sediment. Finally, at the beginning of the simulation, the suspended sediment concentration within the basin is taken to linearly decrease from C_{sea} at the seaward boundary to 0 g/m^3 at the landward boundary.

2.1.3 Bed evolution

Local erosion and deposition drive bed evolution of the channeled and unchanneled portions of the basin. The contribution of bedload to bed evolution is assumed to be much

smaller than the contribution of suspended load. Bed-elevation changes are described through the sediment balance equation (e.g., Marani et al., 2007; Toffolon & Lanzoni, 2010)

$$\frac{\partial z_b}{\partial t} = Q_e - Q_d - R. \tag{13}$$

where Q_e and Q_d are the erosion and deposition rates, respectively and R is the rate of RSLR.

The erosion flux Q_e is determined on the basis of the excess of the shear stress modulus τ with respect to the critical stress τ_{ce}. Conversely, the deposition flux in general depends on the settling velocity and on the magnitude of suspended sediment as clarified in the following.

At each location of the tidal basin the modulus of τ is computed as $\sqrt{\tau_x^2 + \tau_y^2}$, where the components τ_x and τ_y of the bed shear stress vector are determined by considering the local flow depth and the local free surface slope, namely

$$\tau_x = -\rho\, g\, D\, \frac{\partial \zeta}{\partial x}, \qquad \tau_y = -\rho\, g\, D\, \frac{\partial \zeta}{\partial y}. \tag{14}$$

The erosion rate is eventually computed as

$$Q_e = Q_{e0} \left\{ -1 + \left[1 + \left(\frac{\tau}{\tau_{ce}} \right)^4 \right]^{1/4} \right\} \tag{15}$$

where Q_{e0} is a typical intensity of erosion flux, depending on the type of sediment composing the bed. Note that equation (15) ensures a smooth transition from no-erosion to erosion conditions. This formulation, introduced by Carniello et al. (2012), prevents strong gradients of the erosion rate in a neighbourhood of the critical threshold τ_{ce}, thus ensuring a more gradual reproduction of scour processes.

The deposition rate is expressed as (D'Alpaos et al., 2007)

$$Q_d = Q_{ds} + Q_{dt} + Q_{do} \tag{16}$$

where Q_{ds}, Q_{dt} and Q_{do} are the rates of deposition due to settling, vegetation trapping, and organic soil production, respectively. Settling deposition at any shear stress value is computed as

$$Q_{ds} = C\, w_s \tag{17}$$

where w_s is the settling velocity of sediment particles.

On the other hand, trapping deposition and organic deposition are related to vegetation biomass, as described below.

2.1.4 Vegetation growth

The local annually-averaged biomass production is expressed through a fitness function (Marani et al., 2013), which describes the relationship between the local bed elevation z_b and the biomass density $\mathcal{B}$,

$$\frac{\mathcal{B}(z_b)}{\mathcal{B}_{max}} = b(z_b) = \frac{f(z_b)}{f_{max}}, \tag{18}$$

where $\mathcal{B}_{max}$ is the maximum biomass density, $b(z_b)$ is the dimensionless biomass density, $f(z_b)$ is a fitness function and f_{max} is its maximum value. The fitness function is

species specific. Here, following Marani et al. (2013), the fitness function is described through the relation,

$$f(z_b) = \frac{2}{e^{[\lambda_1 (z_b - z_{0v})]} + e^{[-\lambda_2 (z_b - z_{0v})]}}, \tag{19}$$

where the elevation parameter z_{0v} corresponds to the optimal elevation for vegetation growth (i.e. at which the maximum biomass is attained), and the dimensional parameters, λ_1 [m^{-1}] and λ_2 [m^{-1}], control the range of bed elevations to which vegetation is adapted. Large values of λ are typical of specialized vegetation species, that fit within a narrow range of elevations. Conversely, small values of λ characterize species which are relatively well adapted to a broader range of marsh elevations within the tidal frame.

Vegetation patches influence the flow field by modifying the resistance to the flow. A higher biomass density leads to higher friction and, hence, a lower resistance coefficient. The overall bed friction is then assumed to be given by the sum of the local bed friction and the friction induced by the vegetation. This overall bed friction is inversely proportional to the square of a total Gauckler-Strickler resistance coefficient and is expressed as

$$K_s^{-2} = K_{sb}^{-2} + b\, K_{sv}^{-2}, \tag{20}$$

where K_{sb} and K_{sv} are the Gauckler-Strickler coefficients related to bed friction and vegetation, respectively.

Vegetation patches also influence bed evolution by trapping suspended sediment, through stems and leaves, and producing organic soil (the last two terms in equation (16)). Based on the approach of Mudd et al. (2004), Palmer et al. (2004), and D'Alpaos et al. (2006), these contributions to the rate of variation of bed elevation can be expressed as

$$Q_{do} = Q_{do0}\, b(z_b), \tag{21}$$

$$Q_{dt} = C\, U\, \epsilon_v\, d_v\, n_v \min[h_v; D], \tag{22}$$

where Q_{do0} is a typical deposition rate specified empirically and ϵ_v is a capture efficiency coefficient (Palmer et al., 2004). This latter coefficient can in general be related to the diameter d_v, the density n_v and the average height h_v of vegetation stems, as well as to the median suspended sediment size d_{50} through the relation (D'Alpaos et al., 2006)

$$\epsilon = \alpha_\epsilon \left(\frac{U\, d_v}{\nu} \right)^{\beta_\epsilon} \left(\frac{d_{50}}{d_v} \right)^{\gamma_\epsilon} \tag{23}$$

with α_ϵ, β_ϵ and γ_ϵ empirical coefficients.

Finally, the values of the diameter, the density and the average height of vegetation stems can be estimated on the basis of local vegetation biomass through the empirical relations (Mudd et al., 2004, 2010)

$$n_v = \alpha_n\, \mathcal{B}^{\beta_n}, \qquad h_v = \alpha_h\, \mathcal{B}^{\beta_h}, \qquad d_v = \alpha_d\, \mathcal{B}^{\beta_d}. \tag{24}$$

where α_n, β_n, α_h, β_h, α_d and β_d, are empirical coefficients.

2.2 Design of numerical experiments

In this research, we focus on the interactions between tidal channels and vegetation patches that form on a tide-dominated tidal flat of relatively small dimensions, i.e. 400 m wide and 500 m long. Figures 3a-c show the initial bed topography, assumed to be horizontal with small perturbation patches and with a base elevation of 0 m above MSL. The basin is connected with a deep and large tidal channel at the seaward boundary. A square computational grid of size 2 m is used to discretize the relevant equations.

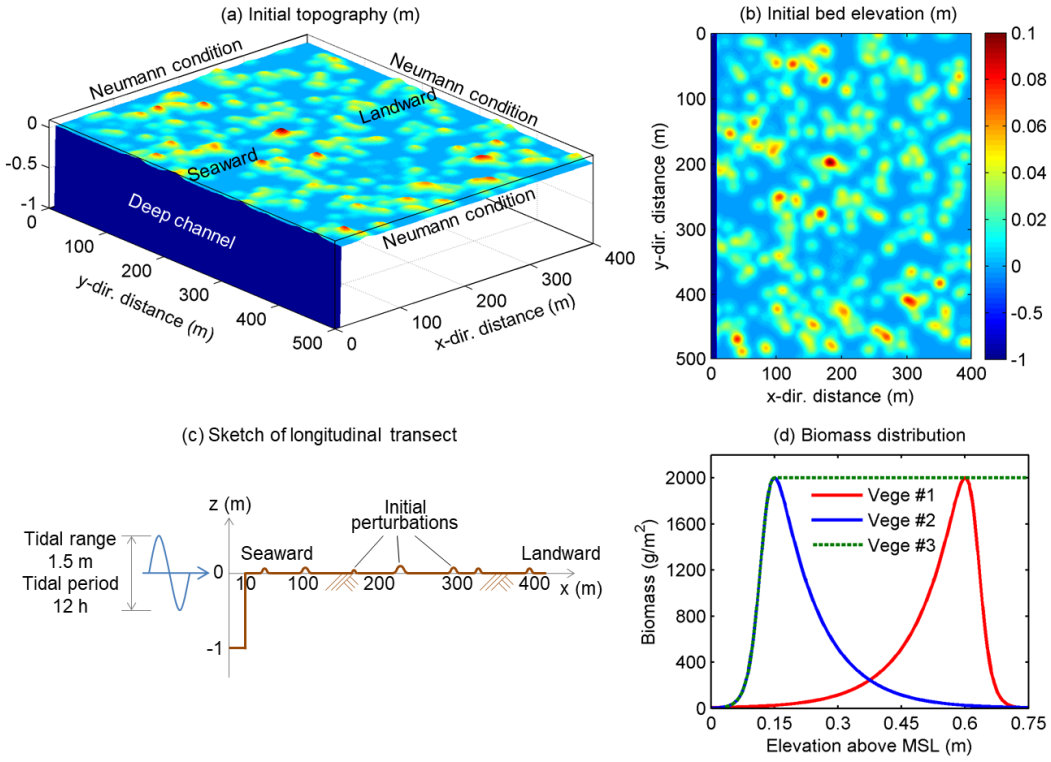

Figure 3. a) Three-dimensional view, b) planform view and c) longitudinal transect of the initial bed topography employed in the present simulations. d) Biomass distribution mimicking three different types of salt-marsh vegetation species.

The initial perturbation patches (in total 450) are generated on a horizontal bed and are meant to mimic the initial settlement of vegetation patches (Figures 3a,b). The location and magnitude of these perturbations are determined by a stochastic procedure. Firstly, the location (x, y) of each perturbation is selected randomly. Secondly, a random height is imposed at each perturbation location. Then, the elevation around the selected point is averaged iteratively to generate a perturbation patch with a smoothly varying surface. This procedure is repeated a certain number of times (15 in the considered case) to expand the patch extension while reducing the patch height, eventually producing relatively isolated perturbation patches. Finally, the maximum elevation of the resulting bed topography is set equal to 0.1 m, and the height of other points is adjusted proportionally. Note that this stochastic procedure leads also to the formation of clustered patches (Figure 3b).

The water level imposed at the seaward boundary reproduces a semi-diurnal tidal cycle of period 12 h and amplitude 0.75 m with respect to MSL (set at 0 m). A no-flux condition is instead prescribed on the other three boundaries of the basin. A sediment concentration C_{sea} of 10 g/m^3 is imposed at seaward boundary during the flood phase of the tide, to mimic an external input of sediment. This input is in general associated with isolated recurrent events (e.g. wind resuspension, spring tides, floods in river nourished environments) but, in the long term, can be modeled imposing a constant (average) C_{sea} as done here.

Because of the significant elevation drop that, during the ebb phase, establishes between the tidal flat and the seaward tidal channel feeding the system (see e.g. Figure 2), extensive erosion spots may take place at the beginning of the morphodynamic evolu-

tion. In order to mitigate these localized phenomena, which may lead to numerical instabilities, the amplitude of the forcing tide is gradually increased from 0 m to 0.75 m within the first 800 tidal cycles.

Typically, a control section forms nearby the seaward border of the tidal basin as the ebb level of the forcing tide becomes smaller than bed elevation (Figure 3c). This section is characterised by a Froude number F_r equal to 1 and disconnects the tidal basin from the seaward channel feeding it. Given this control section, upstream (i.e. landwards) the flow is subcritical ($F_r < 1$), while downstream (i.e. seawards) it is supercritical ($F_r > 1$). The tide level at the seaward boundary thus no longer influences the ebb current still flowing within the tidal basin. The ebb flow is instead controlled by the condition $F_r = 1$ that establishes in the control section. It is thus necessary to modify the seaward boundary condition, by limiting to 1 the corresponding Froude number. During the ebb phase, the effective water depth at the seaward boundary D_{sea} is then prescribed as

$$D_{sea}^{i+1} = \frac{\left|U_{sea}^{i}\right|^2}{0.9\,g}, \qquad \text{If} \qquad F_{r\,sea}^{i} = \frac{\left|U_{sea}^{i}\right|}{\sqrt{g\,D_{sea}^{i}}} > 0.9, \tag{25}$$

where the superscript i indicates the i-th time step and it has been assumed, for computational convenience, that the Froude number at the boundary can be at maximum equal to 0.9. The condition (25) is retained also during the flood phase until the level of the imposed tide exceeds that of the seaward basin border. Henceforth, the flow becomes subcritical everywhere and, hence, is completely controlled by the imposed tidal wave level.

As widely adopted in long-term simulations (Roelvink, 2006; Coco et al., 2013), a morphological factor is used to speed up morphodynamic evolution. After each simulated tidal cycle, the elevation of each computational grid point is first updated through equation (13) and then multiplied by a morphological factor, set equal to 40 after some preliminary tests.

Three different types of vegetation have been considered in the simulations (Figure 3d). All vegetation types start to grow as bed elevation exceeds MSL and survive up to mean high water level (MHWL). The first vegetation type (Vege #1) is better adapted to grow at high elevations. Its biomass increases relatively slowly and reaches a maximum at 0.60 m above MSL. Then biomass decreases rapidly as bed elevation increases, eventually vanishing as MHWL is approached. The second vegetation type (Vege #2) is better adapted to grow at low elevations. Its biomass production peaks at 0.15 m above MSL, i.e. close to MSL, and gradually vanishes towards MHWL. Finally, the third vegetation type (Vege #3) is taken to reproduce biomass distribution in the presence of coexisting vegetation species with optimal biomass production occurring at progressively higher bed elevations (D'Alpaos et al., 2007; Marani et al., 2007). Just above MSL, the biomass function is similar to that of Vege #2. However, after the maximum biomass production is attained (at 0.15 m above MSL), biomass keeps constant.

It is important to note that vegetation seeds cannot settle in areas undergoing intense erosion and, hence, halophytic vegetation is significantly endangered in these areas. Therefore, in present simulations, the local biomass is set to 0 where erosion is stronger than deposition. The values of the physical and empirical parameters adopted in the various simulations are listed in Table 1. Finally, although the parameters for Vege #3 are the same as Vege #2, in the case of Vege #3, the dimensionless biomass density is kept fixed and equal to 1 (green dashed line in Figure 3d) for bed elevations higher than the optimal one (0.15 m).

During the morphodynamic evolution of the basin, tidal channels cut through both tidal flats and salt marshes. The corresponding channelized areas are computed using the channel detection method proposed by Geng et al. (2018).

Table 1. Values of parameters adopted throughout the simulations

Parameter	Value	Parameter	Value
τ_{ce}	0.4 Pa	g	9.81 m/s^2
k_m	0.3 m^2/s	w_s	0.0002 m/s
Q_{e0}	0.0002 m/s	Q_{do0}	0.003 m/yr
e	0.3 m	d_{50}	50 μm
K_{sb}	25 m$^{1/3}$/s	K_{sv}	10 m$^{1/3}$/s
ν	0.000001 m^2/s	α_ϵ	0.224
β_ϵ	0.718	γ_ϵ	2.08
α_n	250 g^{-1}	β_n	0.3032
α_h	0.0609 m^3/g	β_h	0.1876
α_d	0.0006 m^3/g	β_d	0.3
z_{0v}, Vege #1	0.6256	z_{0v}, Vege #2, #3	0.1244
λ_1, Vege #1	60 m^{-1}	λ_1, Vege #2, #3	10 m^{-1}
λ_2, Vege #1	10 m^{-1}	λ_2, Vege #2, #3	60 m^{-1}

3 Results

The initiation and development of tidal channels and the accretion of the intertidal platform are simulated for bare soil conditions and for each of the three vegetation types previously introduced. In the following, we summarize the various morphodynamic processes emerging from the simulations.

3.1 Coupled evolution of salt marshes and tidal channels

At the beginning of each simulation, the tidal amplitude is gradually increasing and has not yet reached its final value. The resulting flow field is relatively weak and hence deposition and erosion rates are quite small. As the tidal amplitude approaches its final value (after 800 tidal cycles, i.e. about 1.1 yr), erosional processes amongst bed perturbation patches gradually increase. Tidal channels start to grow from the seaward boundary through headward erosion after about 2.5 yr and a still immature channel network is visible after about 4 yr (Figures 4a,e,i,m). The structure of this incipient network consists of three main channels with similar spacing and, hence, similar drainage areas. This structure is quite similar for all the simulations, independently of the presence and type of vegetation. Indeed, after 4 yr the elevation of the intertidal platform is still too close to MSL and, when vegetation is considered, the biomass is too small to affect significantly channel morphology.

As the sediment enters the tidal basin through the seaward boundary, the elevation of the intertidal platform progressively increases. The suspended sediment concentration decreases landward, owing to deposition induced by settling and by a progressive decrease of advective transport as prescribed by the advection-diffusion equation (12). The high velocities occurring seaward prompt erosion rates higher than deposition ones. Conversely, proceeding landward, velocities become weaker and hence deposition overcomes erosion.

After their initial growth, channels keep deepening and extending landward, leading to more and more structured channel networks. Perturbation patches prompt channels to curve and to branch diverting or splitting their flows, respectively (Figure 4). This general behaviour is enhanced by vegetation. After 12 yr, channel branching and lengthening occur more frequently in the case of Vege #2 and Vege #3, whose biomass can attain high values also during the early stages of the morphodynamic evolution (Figures

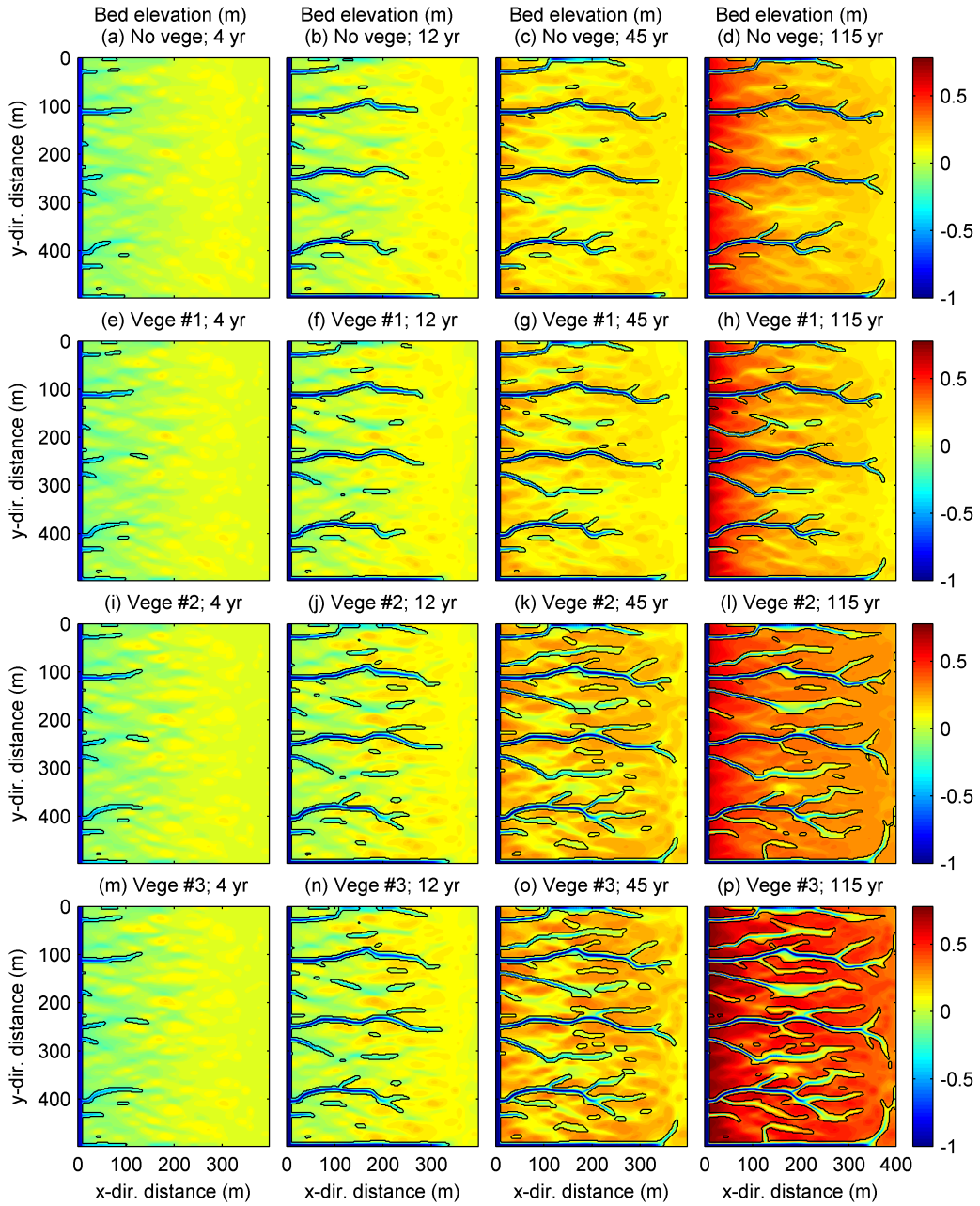

Figure 4. The spatial distribution of bed elevations (m), referred to MSL, is plotted at different evolution stages (4, 12, 45, and 115 yr) for the four simulated cases, i.e. in the absence of vegetation (panels a-d) or in the presence of vegetation (Vege #1, panels e-h; Vege #2, panels i-l; Vege #3, panels m-p). Black lines denote the edge of tidal channels.

5f-h, and j-l). Conversely, in the case of Vege #1, the optimal bed elevation for biomass growth is close to MHWL (Figure 5d) when the channel network has already reached a relatively defined configuration. Consequently, the differences with respect to the channel network obtained without vegetation are less evident (Figures 4b-d, and f-h).

During the bed evolution, platform elevation controls vegetation encroachment and, through the adopted biomass parametrization, its effects on morphology. In the case of Vege #1, as the mean bed elevation of the tidal basin gradually increases, vegetation first starts to encroach seaward areas and then extends landward (Figures 5b-d). This trend is qualitatively similar to that observed in Figure 1b. In the cases of Vege #2 and Vege #3, biomass production is quite high also during the early stages of evolution, when bed elevations are still close to MSL. This allows salt marshes to initially form in the middle and landward areas of the tidal basin, where deposition rates exceed erosion rates. As the intertidal platform emerges on average and exceeds the optimal elevation for biomass, Vege #2, progressively decays (Figures 5f-h). Conversely, Vege #3 gradually spreads throughout the tidal basin (Figures 5j-l) enhancing deposition rates. At the end of the evolution, the mean elevation of the salt marshes is thus higher as compared to the other cases.

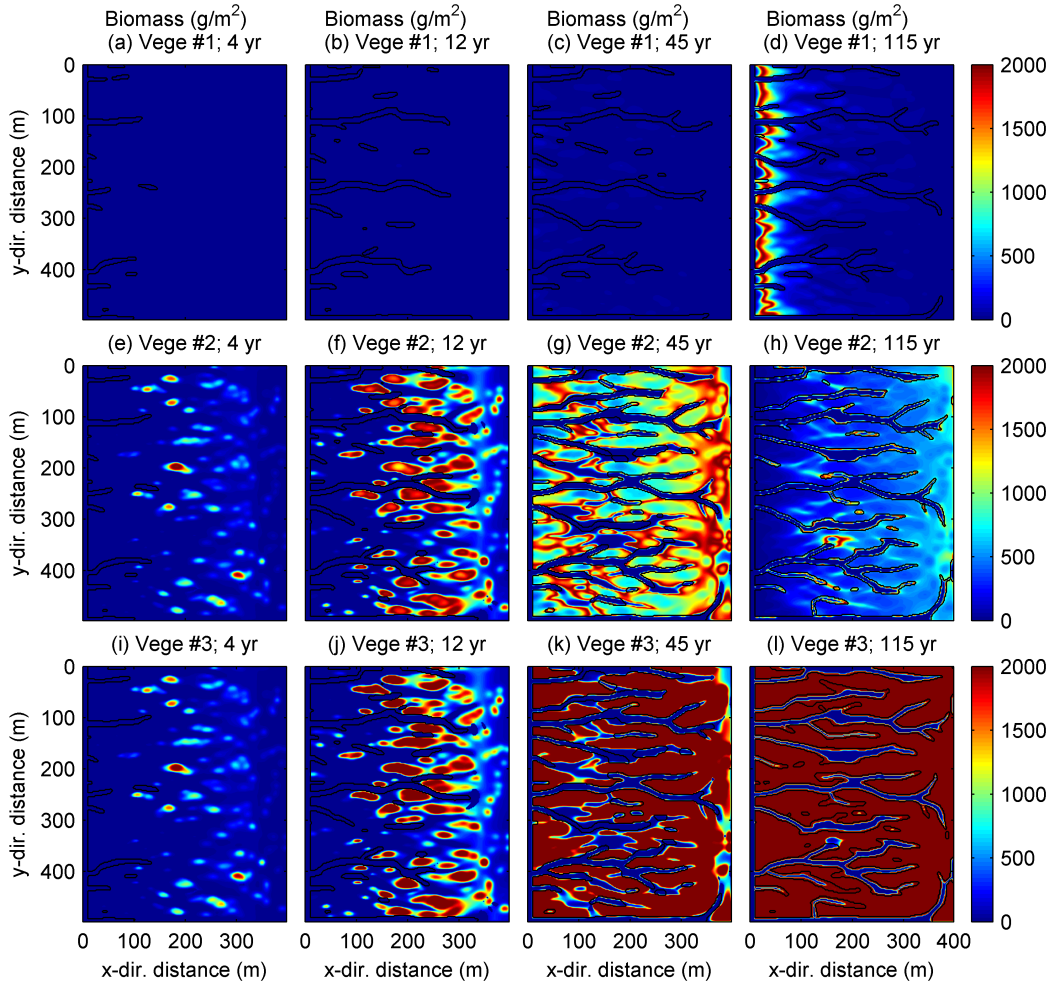

Figure 5. The spatial distribution of vegetation biomass (g/m^2) is plotted at different evolution stages (4, 12, 45, and 115 yr) for the three vegetated cases. Vege #1, Panels a-d; Vege #2, panels e-h; Vege #3, panels i-l.

3.2 Overall vegetation effects

The overall effects of vegetation on the various morphological units, whether channels, marshes or tidal flats, are here evaluated. To this goal, we tracked the temporal evolution of the total vegetation biomass, $\mathcal{B}_T$, the total channel length, L_c, the volume of the channel network, V_c, the mean length of unchanneled flow paths, ℓ, the drainage efficiency ℓ_H/ℓ, and the cumulative amount of erosion $\mathcal{E}_r$.

The total channel length, L_c, is computed by summing the axis length of all the channels cutting through the tidal basin. The total channel volume is defined as the volume between the channel bed and the elevation of the intertidal platform at the channel borders (Geng et al., 2018). The unchanneled flow path length, ℓ, is computed as the mean distance from a point on the intertidal platform to the nearest channel (Marani et al., 2003). The drainage efficiency is given by the ratio ℓ_H/ℓ, with ℓ_H the Hortonian path length given by the ratio of tidal basin area to total channel length (Horton, 1945). For a given Hortonian length, ℓ_H, high values of ℓ_H/ℓ correspond to small values of ℓ, indicating that the spatial arrangement of the tidal channels efficiently reduces the mean overmarsh path length (Marani et al., 2003). Finally, the cumulative erosion $\mathcal{E}_r$ is computed as the total amount of sediment eroded during the evolution.

All the above defined global variables are plotted as a function of time in Figure 6. Both the channel length and the volume of the channel network grow rapidly at the beginning of the evolution (Figures 6a,b). After about 14 yr, as the channels have almost extended throughout the whole tidal basin, the rate of channel lengthening slows down (Figure 6a). As the channels grow landwards, the mean unchanneled length decreases rapidly, eventually tending to a constant value after the total channel length has approached its maximum value (Figure 6c).

The development of vegetation not only promotes channel lengthening (Figure 6a) but also reduces the unchanneled length (Figure 6c). As compared to bare soil conditions, the drainage efficiency of the tidal network increases for vegetation #2 and #3, while it decreases for vegetation #1 (Figure 6d). These findings can be explained by considering the spatial distributions of bed elevation and the channel morphology shown in Figure 4. It emerges that in the case of Vege #1, the final distribution of biomass (Figure 5d) favors the formation of additional channel branches in the seaward and middle portions of the tidal basin (Figure 4h). Conversely, the most landward zones are characterized by a lower degree of channelization, thus leading to a reduction of the overall drainage efficiency of the tidal basin.

In the cases of Vege #2 and Vege #3, the biomass initially reaches quite high values throughout the entire tidal basin (e.g. Figures 5f,j). The tidal channels spread all over the basin and develop many extra branches. Consequently, the drainage efficiency raises (Figure 6d). In particular, the most efficient drainage system is obtained in the case of Vege #3 (Figure 4p) which, at the end of the simulation, exhibits the maximum total biomass as well (Figure 5l). The maximum biomass is approximately four times larger than in the case of Vege #2 (Figure 6d). Indeed, in this latter case, vegetation progressively decays as the bed elevation further accretes after exceeding the optimal level for biomass production. Note that the jumps in drainage efficiency observed for Vege #3 at about 65 yr and 107 yr are associated with the simultaneous headward growth of various channels in the innermost portions of the tidal basin.

It is also worthwhile to note that, during the early stages of evolution (27 yrs), cumulative erosion in the cases of Vege #2 and Vege #3 increases much faster than in the other two cases (Figure 6e). Afterward, differences in cumulative erosion become increasingly smaller and, at the end of the various simulations, tend to vanish. This finding indicates that, even though the final equilibrium configurations of the tidal basin can be

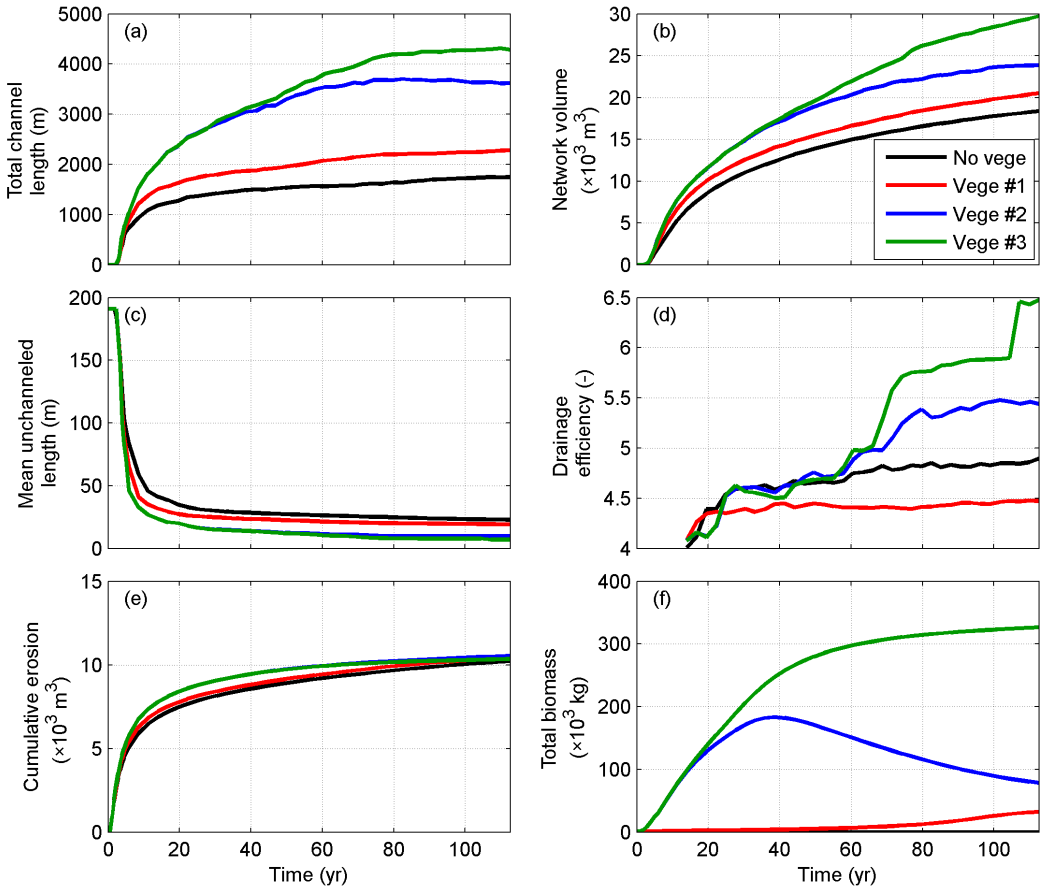

Figure 6. a) The total channel length L_c, b) the total channel volume V_c, c) the mean unchanneled length ℓ, d) the drainage efficiency ℓ_H/ℓ, e) cumulative erosion $\mathcal{E}_r$ and f) the total biomass $\mathcal{B}$ are plotted as a function of time for the simulated tidal channel networks. Black lines denote the bare soil case; red, blue, and green lines denote Vege #1, Vege #2, and Vege 3# cases, respectively.

characterized by different morphologies (Figure 4), they are obtained with almost the same total cumulative erosion.

The distribution of vegetation patches influences the evolution and the overall morphology. The panels in Figures 7a,d,g display the longitudinal variations of mean bed elevation in channeled and unchanneled areas. During the early stage of evolution (12 yrs), mean unchanneled bed elevations exhibit almost similar trends in all the simulations, with an elevation that progressively increases landwards (continuous lines in Figure 7a). Later on, the mean elevation of unchanneled areas becomes higher when vegetation patches spread throughout the entire basin and the biomass is such to yield a significant production of organic soil (Vege #2 and #3, Figure 7d,g). Conversely, for slowly-growing vegetation patches (Vege #1) the differences with respect to the bare soil case are fairly small. Moreover, in the absence of vegetation, the landward portion of the platform is slightly higher than in the vegetated cases. This occurs because vegetation patches in seaward and middle portion of the basin trap the suspended sediment coming from the sea, and thus reduce the amount of sediment delivered landwards leading to lower deposition rates, which is consistent with the field observation results measured in Jiangsu coast, China (Gong et al., 2017). In general, the final equilibrium configuration of the intertidal plat-

form exhibits higher elevations near the sea boundary, it decreases progressively landwards for the first 120 m and then it keeps almost constant or slowly decreasing up to the innermost areas.

The overall morphological variations of channel cross sections can be characterized through the bankfull cross-sectional width and the maximum cross-sectional depth. The along-channel distribution of these quantities is plotted in Figures 7b,e,h and c,f,i with reference to a representative main channel located in the middle of the tidal basin ($y = 200 \sim 300$ m). During its development the channel progressively extends from the seaward border to inner areas of the tidal basin, developing mild bends and minor branches.

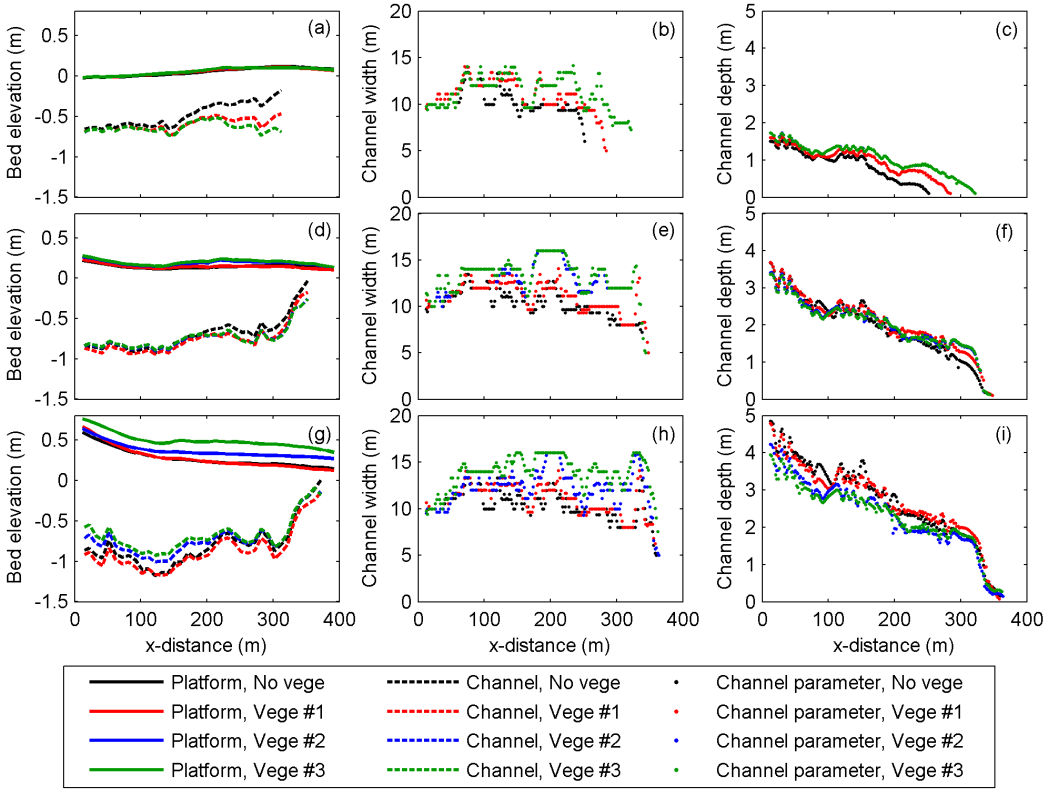

Figure 7. The longitudinal distribution of the mean bed elevation in channelized and unchannelized areas (panels a,d,g), along-channel distribution of cross-sectional width (panels b,e,h), and cross-sectional maximum depth (panels c,f,i) are plotted at different times of the morphodynamic evolution: 12 yr, panels a-c; 45 yr, panels d-f; 115 yr, panels g-i. The cross-sectional parameters are measured from a typical channel located in the middle of the tidal basis. Black dots refer to bare soil while red, blue, and green dots denote Vege #1, Vege #2, and Vege #3, respectively.

A slight narrowing invariably characterizes the cross-sections close to the seaward boundary, where the adjacent unchanneled areas are dominated by deposition. The cross-sectional width then increases as the channel extends in the central region of the tidal basin. Channel width decreases towards the landward channel head (Figures 7b,e,h).

Higher elevations of intertidal areas boosted by vegetation enhance channel widening (blue and green dots in Figures 7e,h). This effect is particularly evident in simulations carried out with Vege #2 and Vege #3. In these two simulations, as compared to Vege #1 and bare soil cases, sediment trapping and organic soil production lead to higher

bed elevations of unchanneled areas in the central and landward portions of the basin (blue and green continuous lines in Figures 7d,g). Instead, near the seaward border, similar channel widths are attained in all four cases. This is due to the intense settling deposition that takes place in this area, which definitely prevails over the contribution of vegetation to sediment deposition.

Channel depth increases over time approaching an almost equilibrium condition as the rate of change in bed elevation tends to vanish. During the first 12 yrs, the channel deepens quite rapidly while extending landwards (Figure 7c). After approximately 45 yr, the channel depth is quite similar for all simulations (Figure 7f). The presence of vegetation eventually (after 115 yr) leads to shallower cross sections in both the seaward and central areas of the basin (Figure 7i). This effect is particularly evident for Vege #2 and Vege #3. The higher mean elevation of the adjacent intertidal platform characterizing these simulations, as compared to the bare soil case, implies that a smaller volume of water needs to be accommodated in channels during the ebb tide. Given also the larger cross-sectional width in the case of Vege #2 and #3 (Figure 7h, blue and green dots), this reduction in the ebb flow discharge explains why the seaward and central reaches of the channel get shallower (Figure 7i).

4 Discussion

4.1 Effects of sea level rise

In coastal areas, intertidal zones are usually influenced by increasing MSL. Mathematical models provide a fundamental tool to evaluate the possible long-term consequences of changes in MSL on tidal eco-morphodynamics. In the case of the schematic tidal basin considered here, keeping fixed all the parameters listed in Table 1, no major differences are observed for relatively low rates of RSLR (2 mm/yr). Conversely, under a fairly large rate of RSLR (8 mm/yr), platform elevations fall below MSL, thus creating unsuitable conditions for vegetation growth.

In the following, we discuss the eco-morphodynamic changes experienced by the investigated tidal basin when subject to a RSLR of 4 mm/yr, close to the value of 3.5 mm/yr usually adopted for the Venice Lagoon in long-term simulations (e.g. Marani et al., 2007). In general, high rates of RSLR and low sediment supplies threaten the development and maintenance of salt marshes. For a given sediment supply, as the rate of RSLR increases, marsh elevation decreases to increase the deposition rate due to the longer hydroperiod, larger water depth and advective transport from the sediment source. However, when marsh elevation falls below a given threshold, vegetation cannot survive and the marsh platform experiences a transition to a tidal flat (Marani et al., 2007; Kirwan & Temmerman, 2009; Kirwan et al., 2010; D'Alpaos et al., 2011). Furthermore, for a given amplitude of the tidal wave, higher mean water depths imply weaker shear stresses and thus smaller erosion rate and longer deposition period. If sediment supply is large enough, bed accretion due to a long-lasting net deposition may keep pace with RSLR, benefiting from the longer hydro-period induced by the rising sea level. On the contrary, a scarce sediment input implies a weaker net deposition, leading to a bed accretion smaller than RSLR (D'Alpaos et al., 2011). Clearly, the spatial distribution of sediment concentration is in general influenced by the basin topography and the related flow patterns. Then, even for a sufficient external sediment supply, different areas within the basin may exhibit contrasting morphological trends in response to RSLR (van der Wegen, 2013; van Maanen et al., 2013). When the sediment input is assumed constant throughout the basin as in some idealized modeling frameworks (e.g. D'Alpaos et al., 2006; Sgarabotto et al., 2021), the differences in the intertidal platform topography are smoothed out and thus these complex evolutionary behaviours cannot be reproduced.

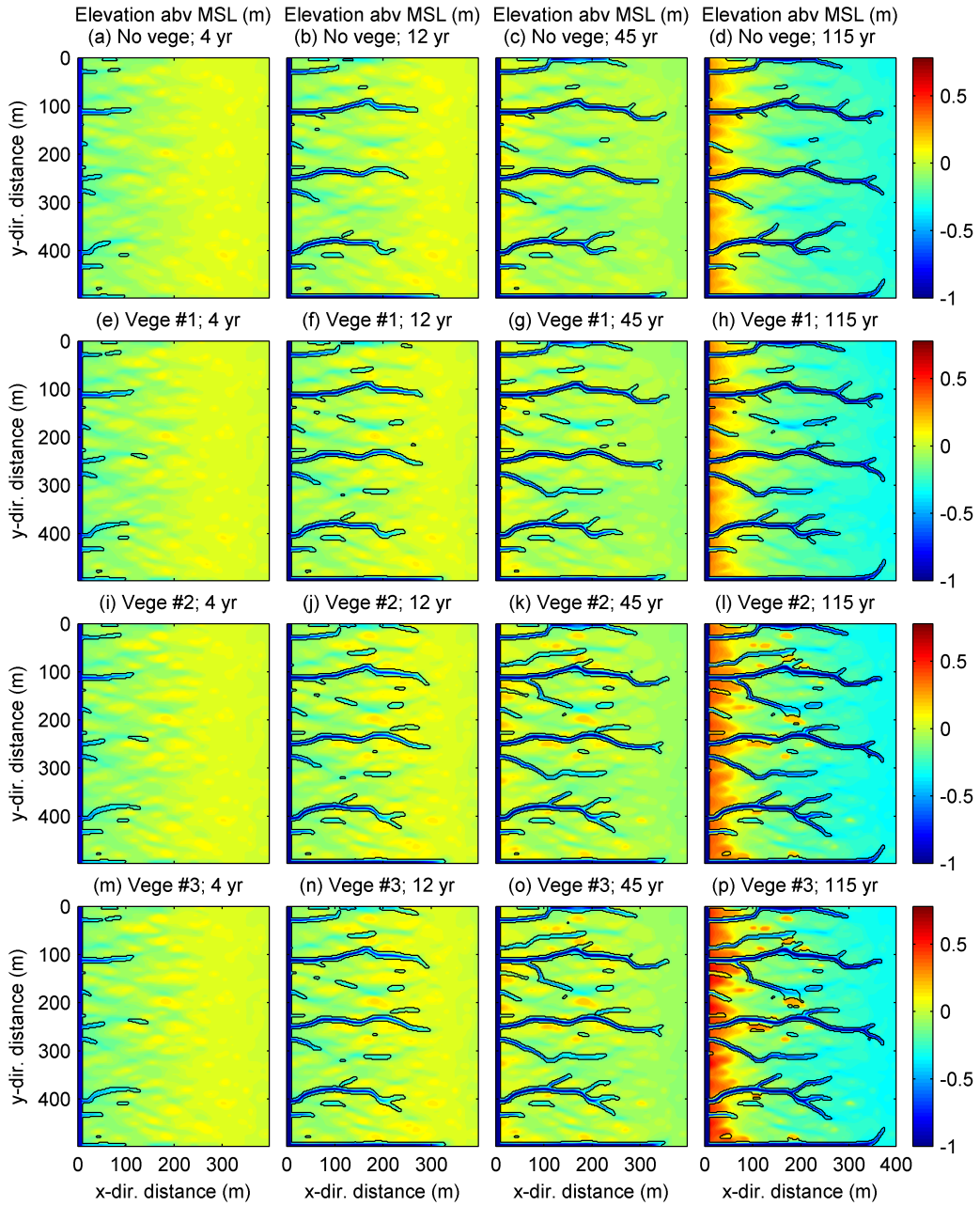

Figure 8. The spatial distribution of bed elevation (m), referred to MSL, is plotted at different evolution stages (4, 12, 45, and 115 yr) for a sea level rise of 4 mm/yr. The four simulated cases, are the same of Figure 4: bare soil, panels a-d; Vege #1, panels e-h; Vege #2, panels i-l; Vege #3, panels m-p. Black lines denote the edge of tidal channels.

Similarly to simulations carried out in the absence of RSLR, tidal channels start to grow from the seaward boundary of the tidal basin and then extend landward through headward erosion. After channel formation, the mean basin elevation gradually increases due to a positive net deposition rate. Vege #2 and Vege #3 patches start to grow throughout the entire basin from the very beginning of the evolution (Figures 8i-l,m-p), while Vege #1 needs higher elevations and, hence, begins to encroach the intertidal platform

later (Figures 8e-h). However, RSLR dramatically restricts vegetation growth in the inner areas of the tidal basin as compared with constant MSL simulations. Indeed, because of the progressive landward decay of the transported sediment, these areas hardly keep pace with the rate of RSLR and become less prone to vegetation growth. Only some vegetation patches with significant biomass survive because of the locally enhanced bed accretion induced by sediment trapping and organic soil production. Outside of these patches, bed accretion is definitely lower and leads to a longer hydroperiod, threatening vegetation survival. Highly vegetated patches thus hardly extend and become increasingly isolated. This uneven spatial distribution of vegetation exacerbates the differences in topography across the tidal basin. Eventually, vegetation biomass inevitably concentrates near the seaward border, where higher bed elevations are attained. The basin thus develops a remarkable landward-decreasing bed slope (Figures 8d,h,l,p).

The overall effects of RSLR on tidal-channel and marsh morphology are shown in Figure 9 in terms of total channel length and total biomass. In the unvegetated case, the increasing mean sea level has little influence on the development of the tidal channel networks, at least for the present schematic basin. As compared with the case with no RSLR (Figure 6a), the total channel length measured at the end of the simulation increases slightly, by about 2.1%.

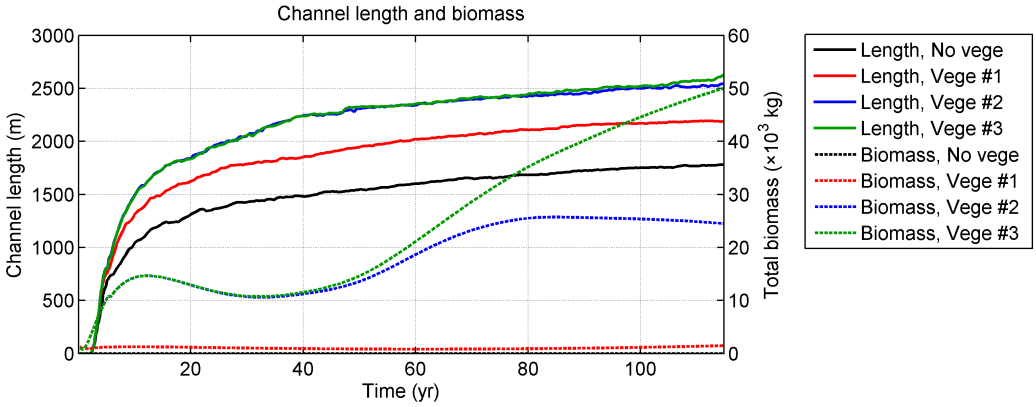

Figure 9. Variations in total channel length (continuous lines) and total biomass (dotted lines) are plotted versus time for the various cases considered in the simulations carried out with a sea level rise of 4 mm/yr. Black lines denote the bare soil case; red, blue, and green lines denote Vege #1, Vege #2 and Vege #3 cases, respectively.

On the contrary, RSLR has a strong impact on total vegetation growth. Indeed, owing to the overall lower relative bed elevation, vegetation biomass is remarkably smaller than in simulations carried out with a constant MSL (Figure 6f). As a result, vegetation affects the development of tidal channels to a less extent. The total biomass of Vege #1 is an order of magnitude smaller than that of Vege #2 and Vege #3. Vegetation growth concentrates near the seaward border of the basin where, as shown in Figure 8h, higher bed elevations ultimately occur. The total channel length is about 4% shorter than that observed in the case of a constant MSL.

Also for the other two vegetation types, RSLR causes a remarkable decrease of total biomass, which at the end of the simulations turns out to be approximately six times (Vege #2) and four times (Vege #3) smaller than in the case of a constant MSL (Figure 6f, blue and green lines). Total biomass reduction is particularly severe in the period between 14 and 34 yr when vegetation patches, initially grown in the inner portions

of the tidal basin, progressively decrease in size owing to the reduced accretion rate of the intertidal platform. In both cases, similarly to Vege #1, biomass eventually concentrates near the seaward basin border. As compared to the bare soil situation, the influence of Vege #2 and Vege #3 on the tidal channel morphology is fairly similar and prompts a slight increase (about 43 %) in the total channel length.

4.2 Comparison with field data

Multiple environmental factors influence the development of tidal channel networks, leading to a wide range of structures and patterns. In the absence of detailed information on the boundary conditions and on the past changes in landforming processes occurred within an intertidal environment, it is almost impossible to reproduce numerically the actual morphology of a tidal channel system. A general comparison between the features of real and synthetic channel patterns may however be based on some relevant statistics (e.g. the mean channel width and length, and the mean channel spacing).

As previously stated, in the present contribution we focus on small tidal environments connecting with large channels as those shown in Figure 1, concerning the south edge of Warbah Island (Shatt el-Arab Estuary, Kuwait), the Great Ouse River (The Wash, UK), the Petaluma River (California, USA), and the Dell'Ancora Channel (Venice Lagoon, IT). Note that, while Warbah Island is characterized by channels cutting through bare tidal flats, the other three cases instead refer to salt-marsh channels.

In particular, we applied the model to mimic the fearures of tidal channels forming in the rectangular areas depicted with red lines in Figures 1a,b. The tidal basin considered in Warbah Island (hereafter denoted with WI) has a length of 600 m and a width of 500 m. In Kuwait Bay, the tides are semidiurnal and the tidal range changes from 4.2 m (during spring tides) to 0.5 m (during neap tides) (Baby, 2011). Considering the cosine tide wave used in the simulation, the tidal range is set to 2 m. Given the lack of specific information, the seaward sediment concentration is tentatively set to 10 g/m^3, corresponding to the lower SSC values observed in the northwest Persian Gulf (Al-Ghadban, 2004; Al-Yamani et al., 2004). In the case of the salt marsh flanking the Dell'Ancora channel in the Venice lagoon (hereafter denoted as VE), the tidal basin length is 80 m and the width is 50 m. Similar to other studies carried out for the Venice Lagoon (D'Alpaos & Marani, 2016), the tidal forcing is taken to be sinusoidal with amplitude of 0.5 m. The input sediment concentration is set to 3 g/m^3, and kept constant in time. This value has been taken lower than the sediment concentration measured in the neighboring area (about 8.6 g/m^3, Carniello et al., 2012; Venier et al., 2014) to account for the intermittency of the wind-events leading to the observed concentration value. Two vegetation scenarios are considered. Typically, salt marshes in the Venice Lagoon are colonized by multiple species vegetation (Silvestri et al., 2005; D'Alpaos et al., 2007). Vegetation biomass then attains high values even when bed elevation reaches relatively high levels. Here, for sensitivity analysis purposes, two different biomass functions (Vege #VE1 and Vege #VE2) have been considered to mimic a multiple species vegetation (Figure 10d). In both cases, the biomass is kept fixed after its maximum is attained for a prescribed elevation (0.4 m above MSL for Vege #VE1, and 0.1 m above MSL for Vege #VE2). Simulations lasted 115 yr, such that the channels and the surrounding intertidal platform have approximately reached a stable configuration characterized by a vanishing small rate of morphological changes.

Figures 10a-c show the bed topographies at the end of the simulations. Almost parallel channels grow within the simulated basins, as observed in the field (Figures 10e,f). However, compared with the actual channels the numerically generated channels have fewer branches. This finding is possibly related to the grid size (2 m for simulation WI

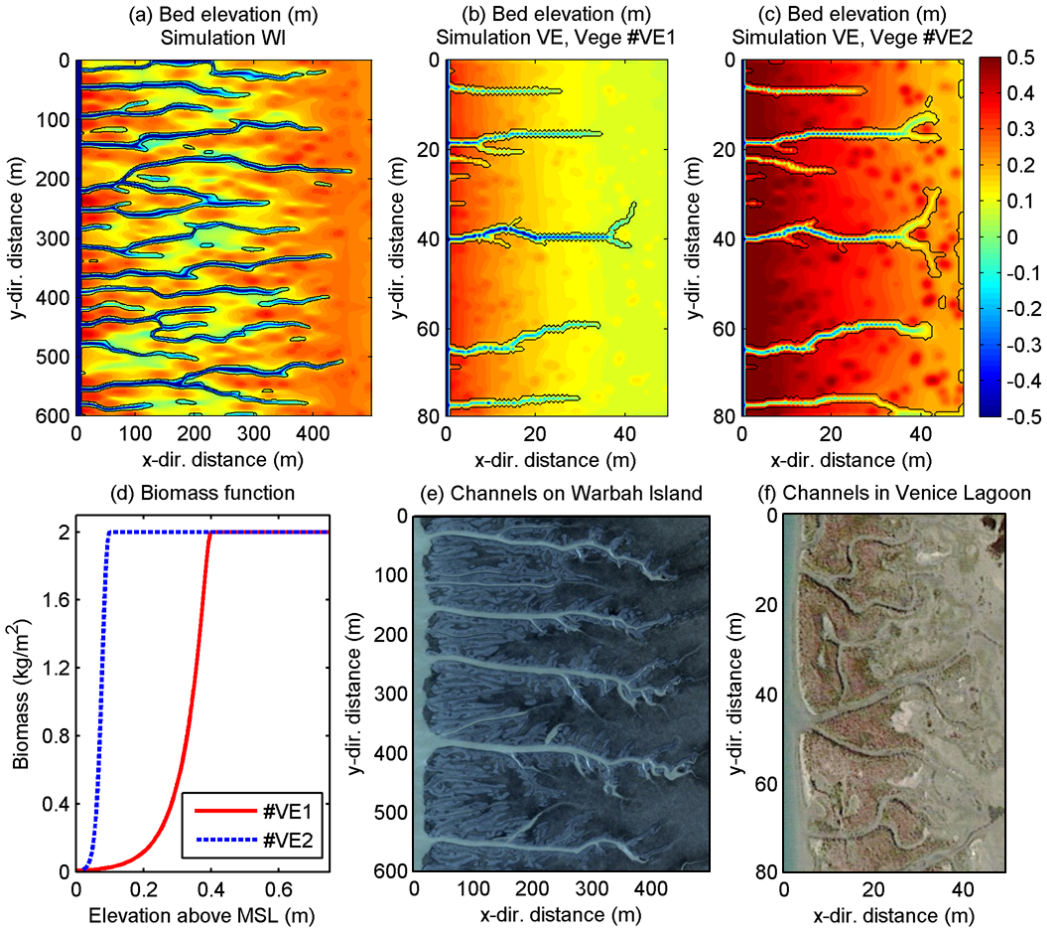

Figure 10. The bed topography (expressed in m) obtained after 115 yr in the simulations carried out for a) Warbah Island and b,c) a typical small salt marsh in the Venice lagoon. In this latter case, two different type of vegetation have been considered, Vege #VE1 and Vege #VE2, with biomass functions shown in plot d). (e-f) Enlarged view of the actual channel morphologies observed in WI and VE.

and 0.5 m for simulations VE) and the initial bed perturbations used in the simulations, which limit the formation of smaller branches.

In the case of the VE marsh, the mean length, mean width and mean spacing (both measured at the seaward border) of simulated channels are definitely similar to the actual ones (Figure 11). Channel features strongly depend on the size of the tidal basin. Indeed, the Venice channels investigated here are definitely narrower than synthetic channels recently reproduced in Sgarabotto et al. (2021) where mean channel width reaches 20 m in a basin 100 times larger than that here considered. In the case of WI, simulated channels are generally wider and have a larger spacing as compared to channels observed in the field. Note that in the simulations the channel length is likely related to the imposed basin length, which exerts some control on the volume of water to be drained during every ebb tide.

Clearly, various uncertainties affect the parameters used in the simulations, especially for WI (e.g. the externally imposed concentration, the critical shear stresses for erosion, initial bed perturbations). These uncertainties might in part explain why the

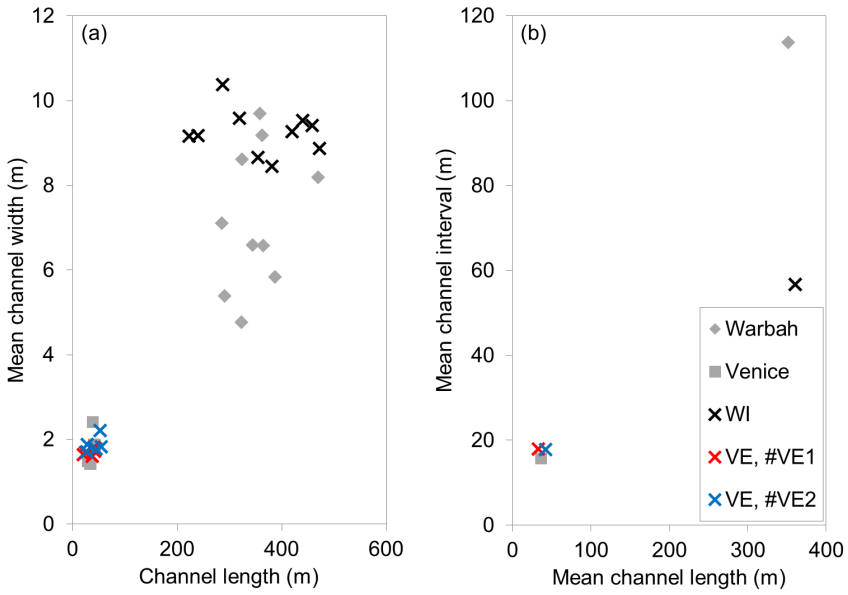

Figure 11. a) Mean channel width and b) mean channel interaxis are plotted versus mean channel length for observed and numerically generated tidal channels shown in Figure 10.

simulated WI channels exhibit a smaller range of width values as compared to reality. Certainly, the simulated environmental conditions are simpler and more homogeneous than in the field. Besides, near bank flow, and hence bank erosion, are poorly represented in the model. The initial bed topography can also affect the channel network morphology. The initial randomly generated disturbances superposed to an otherwise horizontal bed may influence the final channel network geometry, leading in the case of WI to less spaced channels than in the field.

4.3 Model limitations

The present modeling framework is based on some relevant assumptions. First, friction is assumed to dominate over inertia (Rinaldo et al., 1999) in the momentum equations. Nevertheless, inertia can play an important role within the channels as well as near vegetation patches, leading to longer wakes behind them (Van Oyen et al., 2014). Second, erosion at the channel banks and at the seaward border of the tidal basin is described approximately as a continuous process. No sub-grid parameterization is used to account for the actual shape of the bank/border and of localized and intermittent bank collapse events. These approximations have surely an influence on channel width computations. Then the condition (25) imposed at the seaward boundary to limit the Froude number during late ebb and early flood may have some influence on the morphology eventually attained by the seaward border of the tidal basin. Wave-induced erosion, not accounted for in the model, may also matter even in the presence of a vegetated platform (e.g. Marani et al., 2011; Mariotti & Fagherazzi, 2013; Leonardi & Fagherazzi, 2014; Leonardi et al., 2016). Finally, the offline technique for the bed update may affect the synthetic morphologies. Overall, despite the simplifications introduced with respect to 2-D morphodynamic models (Hibma et al., 2003; Van der Wegen & Roelvink, 2008; Coco et al., 2013; Boelens et al., 2018), the present model is deemed to reproduce correctly the eco-morphodynamic evolution of the various morphological units composing small tidal basins, producing tidal morphologies which reasonably resemble those observed in the field.

5 Conclusions

This study focused on the eco-morphodynamic co-evolution of tidal channels and salt marshes in a schematic basin, mimicking tidal environments flanking large tidal channels or tidal rivers. The co-evolution is simulated through a bio-morphodynamic model which accounts for wetting-and-drying processes and vegetation-induced roughness. Different types of vegetation have been considered, each characterized by a specific biomass function depending on bed elevation. Simulations have been carried out by letting the system evolve starting from a horizontal, slightly and randomly-perturbed bed, under the influence of a forcing tide and a sediment concentration imposed at the seaward boundary. The main results of our analysis can be summarized as follows.

Model results successfully mimic the morphologies observed in the field for both bare soil and vegetated conditions. In general, widely spread vegetation patches are found to definitely affect the structure of the tidal channel network. The increased friction produced by vegetation feeds back on the flow field and, consequently, on the erosion and deposition patterns that ultimately determine the structure of the tidal channel network.

Vegetation with an optimal elevation for biomass production close to MSL is found to strongly promote the development of tidal channels as compared with the bare soil case. Specifically, channels extend more rapidly landward, through headward erosion. Their cross sections are usually wider and shallower. In addition, more channel branches grow, forming more complex network structures with a higher drainage efficiency with respect to the bare soil case, as well as to the case of vegetation with a higher optimal elevation for biomass production.

In general, vegetation starts to colonize the intertidal platform from the seaward border, where the externally supplied sediment concentration ensures a more rapid bed accretion. Vegetation then extends landwards. The presence of pioneer vegetation (mimicked by introducing randomly distributed perturbations of the initial bed topography) enhances the deposition on unchanneled areas, leading to faster growth of salt marshes, especially for species with optimal biomass production occurring closer to MSL. Vegetation trapping of suspended sediment in the seaward and middle portions of the tidal basin invariably reduces the amount of sediment delivered to landward areas, weakening the sedimentation there.

In the presence of RSLR, owing to the lower relative bed elevation above MSL, vegetation growth is limited and, consequently, its control on channel morphology is reduced. Given a sufficient seaward sediment supply, the deposition rate at the seaward border of the basin can keep pace with the rate of RSLR. Conversely, the inner basin becomes incrementally submerged and a landward bed slope forms. Vegetation patches with high biomass become increasingly isolated. Indeed, the bare tidal platform adjacent to these patches experiences a deposition rate much lower than that needed to counteract the effect of RSLR.

The simulated channel networks exhibit a reasonable similarity with the parallel channel patterns observed in tidal areas adjacent to larger tidal channels. Nevertheless, the simulated cross sections are somewhat wider than those observed in the field, especially the smaller channel branches. This finding is strictly related to the relatively large grid size used in the simulations, which prevents reproducing correctly the smaller creek geometry. Clearly, the lack of a sub-grid parametrization of bank erosion and bank collapse events can also explain the differences between simulated and real channel geometries.

Data Availability Statement

The data used in the current study are available at https://doi.org/10.5281/zenodo.5075102.

Acknowledgments

This research was supported by the University of Padova, by the ICEA department within the University of Padova and by National Natural Science Foundation of China (51620105005 and 51879095). Liang Geng acknowledges the China Scholarship Council (CSC) for the support of doctoral study. We would like to express our very great appreciation to Prof. Tomas Van Oyen from Ghent University and Prof. Mario Putti from the University of Padova for their support and suggestions on this model.

References

Al-Ghadban, A. N. (2004). Assessment of suspended sediment in Kuwait Bay using Landsat and SPOT images. *Kuwait Journal of Science and Engineering*, *31*(2), 155–172.

Allen, J. R. (2000). Morphodynamics of holocene salt marshes: A review sketch from the Atlantic and Southern North Sea coasts of Europe. *Quaternary Science Reviews*, *19*(12), 1155–1231.

Al-Yamani, F. Y., Bishop, J., Ramadhan, E., Al-Husaini, M., & Al-Ghadban, A. N. (2004). *Oceanographic atlas of Kuwait's waters*. Kuwait: Kuwait Institute for Scientific Research.

Baby, S. (2011). Information research on coastal morphological environment of Kuwait, organizations, role and coastal legislations. *Emirates Journal for Engineering Research*, *16*(2), 7–24.

Balke, T., Bouma, T. J., Horstman, E. M., Webb, E. L., Erftemeijer, P. L., & Herman, P. M. (2011). Windows of opportunity: Thresholds to mangrove seedling establishment on tidal flats. *Marine Ecology Progress Series*, *440*, 1–9.

Balke, T., Herman, P. M., & Bouma, T. J. (2014). Critical transitions in disturbance-driven ecosystems: Identifying Windows of Opportunity for recovery. *Journal of Ecology*, *102*(3), 700–708.

Belliard, J.-P., Toffolon, M., Carniello, L., & D'Alpaos, A. (2015). An ecogeomorphic model of tidal channel initiation and elaboration in progressive marsh accretional contexts. *Journal of Geophysical Research: Earth Surface*, *120*(6), 1040–1064.

Bendoni, M., Mel, R., Solari, L., Lanzoni, S., Francalanci, S., & Oumeraci, H. (2016). Insights into lateral marsh retreat mechanism through localized field measurements. *Water Resources Research*, *52*, 1446–1464.

Boelens, T., Schuttelaars, H., Schramkowski, G., & De Mulder, T. (2018). The effect of geometry and tidal forcing on hydrodynamics and net sediment transport in semi-enclosed tidal basins. *Ocean Dynamics*, *68*(10), 1285–1309.

Bouma, T. J., van Belzen, J., Balke, T., Zhu, Z., Airoldi, L., Blight, A. J., … Herman, P. M. (2014). Identifying knowledge gaps hampering application of intertidal habitats in coastal protection: Opportunities & steps to take. *Coastal Engineering*, *87*, 147–157.

Carniello, L., Defina, A., & D'Alpaos, L. (2012). Modeling sand-mud transport induced by tidal currents and wind waves in shallow microtidal basins: Application to the Venice Lagoon (Italy). *Estuarine, Coastal and Shelf Science*, *102*, 105–115.

Chen, X., Zhang, C., Paterson, D., Thompson, C., Townend, I., Gong, Z., … Feng, Q. (2017). Hindered erosion: The biological mediation of noncohesive sediment behavior. *Water Resources Research*, *53*(6), 4787–4801.

Coco, G., Zhou, Z., van Maanen, B., Olabarrieta, M., Tinoco, R., & Townend, I. (2013). Morphodynamics of tidal networks: Advances and challenges. *Marine Geology*, *346*, 1–16.

Cowell, P., & Thom, B. (1994). Morphodynamics of coastal evolution. In R. Carter & C. Woodroffe (Eds.), *Coastal evolution: Late Quaternary shoreline morphodynamics* (pp. 33–86). Cambridge University Press, Cambridge.

D'Alpaos, A., Lanzoni, S., Marani, M., Fagherazzi, S., & Rinaldo, A. (2005). Tidal network ontogeny: Channel initiation and early development. *Journal of Geophysical Research: Earth Surface*, *110*(F02001), 1–14.

D'Alpaos, A., Lanzoni, S., Marani, M., & Rinaldo, A. (2007). Landscape evolution in tidal embayments: Modeling the interplay of erosion, sedimentation, and vegetation dynamics. *Journal of Geophysical Research: Earth Surface*, *112*(F01008), 1–17.

D'Alpaos, A., Lanzoni, S., Mudd, S. M., & Fagherazzi, S. (2006). Modeling the influence of hydroperiod and vegetation on the cross-sectional formation of tidal channels. *Estuarine, Coastal and Shelf Science*, *69*(3-4), 311–324.

D'Alpaos, A., & Marani, M. (2016). Reading the signatures of biologic–geomorphic feedbacks in salt-marsh landscapes. *Advances in water resources*, *93*, 265–275.

D'Alpaos, A., Mudd, S. M., & Carniello, L. (2011). Dynamic response of marshes to perturbations in suspended sediment concentrations and rates of relative sea level rise. *Journal of Geophysical Research: Earth Surface*, *116*(F04020), 1–13.

Defina, A. (2000). Two-dimensional shallow flow equations for partially dry areas. *Water resources research*, *36*(11), 3251–3264.

De Swart, H., & Zimmerman, J. (2009). Morphodynamics of tidal inlet systems. *Annual review of fluid mechanics*, *41*, 203–229.

Fagherazzi, S., Carniello, L., D'Alpaos, L., & Defina, A. (2006). Critical bifurcation of shallow microtidal landforms in tidal flats and salt marshes. *Proceedings of the National Academy of Sciences*, *103*(22), 8337–8341.

Fagherazzi, S., Gabet, E. J., & Furbish, D. J. (2004). The effect of bidirectional flow on tidal channel planforms. *Earth Surface Processes and Landforms*, *29*(3), 295–309.

FitzGerald, D. M., & Hughes, Z. (2019). Marsh processes and their response to climate change and sea-level rise. *Annual Review of Earth and Planetary Sciences*, *47*, 481–517.

Friedrichs, C. T., & Perry, J. E. (2001). Tidal salt marsh morphodynamics: A synthesis. *Journal of Coastal Research*, 7–37.

Geng, L., Gong, Z., Lanzoni, S., & D'Alpaos, A. (2018). A new method for automatic definition of tidal creek networks. *Journal of Coastal Research*(85), 156–160.

Gong, Z., Jin, C., Zhang, C., Zhou, Z., Zhang, Q., & Li, H. (2017). Temporal and spatial morphological variations along a cross-shore intertidal profile, Jiangsu, China. *Continental Shelf Research*, *144*, 1–9.

Gong, Z., Zhao, K., Zhang, C., Dai, W., Coco, G., & Zhou, Z. (2018). The role of bank collapse on tidal creek ontogeny: A novel process-based model for bank retreat. *Geomorphology*, *311*, 13–26.

Hibma, A., Schuttelaars, H. M., & Wang, Z. B. (2003). Comparison of longitudinal equilibrium profiles of estuaries in idealized and process-based models. *Ocean Dynamics*, *53*(3), 252–269.

Horton, R. E. (1945). Erosional development of streams and their drainage basins; hydrophysical approach to quantitative morphology. *Geological society of America bulletin*, *56*(3), 275–370.

Hu, Z., van Belzen, J., van Der Wal, D., Balke, T., Wang, Z. B., Stive, M., & Bouma, T. J. (2015). Windows of opportunity for salt marsh vegetation establishment on bare tidal flats: The importance of temporal and spatial variability in hydrodynamic forcing. *Journal of Geophysical Research: Biogeosciences*, *120*(7), 1450–1469.

Hughes, Z. J. (2012). Tidal channels on tidal flats and marshes. In R. A. Davis Jr & R. W. Dalrymple (Eds.), *Principles of tidal sedimentology* (pp. 269–300). Springer.

Kirwan, M. L., Guntenspergen, G. R., D'Alpaos, A., Morris, J. T., Mudd, S. M., & Temmerman, S. (2010). Limits on the adaptability of coastal marshes to rising

781 sea level. *Geophysical research letters*, *37*(L23401), 1–5.
782 Kirwan, M. L., & Megonigal, J. P. (2013). Tidal wetland stability in the face of hu-
783 man impacts and sea-level rise. *Nature*, *504*(7478), 53–60.
784 Kirwan, M. L., & Temmerman, S. (2009). Coastal marsh response to historical
785 and future sea-level acceleration. *Quaternary Science Reviews*, *28*(17-18),
786 1801–1808.
787 Kleinhans, M. G., van Scheltinga, R. T., van Der Vegt, M., & Markies, H. (2015).
788 Turning the tide: Growth and dynamics of a tidal basin and inlet in experi-
789 ments. *Journal of Geophysical Research: Earth Surface*, *120*(1), 95–119.
790 Lawrence, D., Allen, J. R., & Havelock, G. (2004). Salt marsh morphodynamics: An
791 investigation of tidal flows and marsh channel equilibrium. *Journal of Coastal*
792 *Research*, *20*(1), 301–316.
793 Leonardi, N., & Fagherazzi, S. (2014). How waves shape salt marshes. *Geology*,
794 *42*(10), 887–890.
795 Leonardi, N., Ganju, N. K., & Fagherazzi, S. (2016). A linear relationship between
796 wave power and erosion determines salt-marsh resilience to violent storms and
797 hurricanes. *Proceedings of the National Academy of Sciences*, *113*(1), 64–68.
798 Li, X., Leonardi, N., & Plater, A. J. (2019). A stochastic approach to modeling
799 tidal creek evolution: Exploring environmental influences on creek topologies
800 through ensemble predictions. *Geophysical Research Letters*, *46*(23), 13836–
801 13844.
802 Lovelock, C. E., Bennion, V., Grinham, A., & Cahoon, D. R. (2011). The role of
803 surface and subsurface processes in keeping pace with sea level rise in intertidal
804 wetlands of Moreton Bay, Queensland, Australia. *Ecosystems*, *14*(5), 745–757.
805 Marani, M., Belluco, E., D'Alpaos, A., Defina, A., Lanzoni, S., & Rinaldo, A.
806 (2003). On the drainage density of tidal networks. *Water Resources Research*,
807 *39*(2), 1040.
808 Marani, M., Da Lio, C., & D'Alpaos, A. (2013). Vegetation engineers marsh mor-
809 phology through multiple competing stable states. *Proceedings of the National*
810 *Academy of Sciences*, *110*(9), 3259–3263.
811 Marani, M., D'Alpaos, A., Lanzoni, S., Carniello, L., & Rinaldo, A. (2007).
812 Biologically-controlled multiple equilibria of tidal landforms and the fate of
813 the Venice Lagoon. *Geophysical Research Letters*, *34*(L11402), 1–5.
814 Marani, M., D'Alpaos, A., Lanzoni, S., & Santalucia, M. (2011). Understanding
815 and predicting wave erosion of marsh edges. *Geophysical Research Letters*,
816 *38*(L21401), 1–5.
817 Marani, M., Lanzoni, S., Zandolin, D., Seminara, G., & Rinaldo, A. (2002). Tidal
818 meanders. *Water Resources Research*, *38*(11), 1–14.
819 Mariotti, G. (2018). Marsh channel morphological response to sea level rise and sed-
820 iment supply. *Estuarine, Coastal and Shelf Science*, *209*, 89–101.
821 Mariotti, G., & Fagherazzi, S. (2013). Critical width of tidal flats triggers marsh
822 collapse in the absence of sea-level rise. *Proceedings of the national Academy of*
823 *Sciences*, *110*(14), 5353–5356.
824 Mitsch, W. J., & Gosselink, J. G. (2000). The value of wetlands: Importance of scale
825 and landscape setting. *Ecological Economics*, *35*(1), 25–33.
826 Morris, J. T., Sundareshwar, P., Nietch, C. T., Kjerfve, B., & Cahoon, D. R. (2002).
827 Responses of coastal wetlands to rising sea level. *Ecology*, *83*(10), 2869–2877.
828 Mudd, S. M., D'Alpaos, A., & Morris, J. T. (2010). How does vegetation affect
829 sedimentation on tidal marshes? Investigating particle capture and hydrody-
830 namic controls on biologically mediated sedimentation. *Journal of Geophysical*
831 *Research: Earth Surface*, *115*(F03029), 1–14.
832 Mudd, S. M., Fagherazzi, S., Morris, J. T., & Furbish, D. J. (2004). Flow, sedimen-
833 tation, and biomass production on a vegetated salt marsh in South Carolina:
834 Toward a predictive model of marsh morphologic and ecologic evolution. In
835 S. Fagherazzi, A. Marani, & L. Blum (Eds.), *The ecogeomorphology of tidal*

marshes, coastal estuarine stud (Vol. 59, pp. 165–187). AGU, Washington, D. C.

Palmer, M. R., Nepf, H. M., Pettersson, T. J., & Ackerman, J. D. (2004). Observations of particle capture on a cylindrical collector: Implications for particle accumulation and removal in aquatic systems. *Limnology and Oceanography*, *49*(1), 76–85.

Pilkey, O. H., & Cooper, J. A. G. (2004). Society and sea level rise. *Science*, *303*(5665), 1781–1782.

Rinaldo, A., Fagherazzi, S., Lanzoni, S., Marani, M., & Dietrich, W. E. (1999). Tidal networks: 2. Watershed delineation and comparative network morphology. *Water Resources Research*, *35*(12), 3905–3917.

Roelvink, J. (2006). Coastal morphodynamic evolution techniques. *Coastal engineering*, *53*(2-3), 277–287.

Sgarabotto, A., D'Alpaos, A., & Lanzoni, S. (2021). Effects of vegetation, sediment supply and sea level rise on the morphodynamic evolution of tidal channels. *Water Resources Research*(e2020WR028577), 1–24.

Silvestri, S., Defina, A., & Marani, M. (2005). Tidal regime, salinity and salt marsh plant zonation. *Estuarine, coastal and shelf science*, *62*(1-2), 119–130.

Stefanon, L., Carniello, L., D'Alpaos, A., & Rinaldo, A. (2012). Signatures of sea level changes on tidal geomorphology: Experiments on network incision and retreat. *Geophysical Research Letters*, *39*(L12402), 1–6.

Temmerman, S., Bouma, T., van de Koppel, J., van der Wal, D., De Vries, M., & Herman, P. (2007). Vegetation causes channel erosion in a tidal landscape. *Geology*, *35*(7), 631–634.

Temmerman, S., Bouma, T. J., Govers, G., Wang, Z. B., De Vries, M., & Herman, P. (2005). Impact of vegetation on flow routing and sedimentation patterns: Three-dimensional modeling for a tidal marsh. *Journal of Geophysical Research: Earth Surface*, *110*(F04019), 1–18.

Temmerman, S., Moonen, P., Schoelynck, J., Govers, G., & Bouma, T. J. (2012). Impact of vegetation die-off on spatial flow patterns over a tidal marsh. *Geophysical Research Letters*, *39*(L03406), 1–5.

Toffolon, M., & Lanzoni, S. (2010). Morphological equilibrium of short channels dissecting the tidal flats of coastal lagoons. *Journal of Geophysical Research: Earth Surface*, *115*(F04036), 1–15.

Tommasini, L., Carniello, L., Ghinassi, M., Roner, M., & D'Alpaos, A. (2019). Changes in the wind-wave field and related salt-marsh lateral erosion: Inferences from the evolution of the Venice Lagoon in the last four centuries. *Earth Surface Processes and Landforms*, *44*(8), 1633–1646.

Toy, T. J., Foster, G. R., & Renard, K. G. (2002). *Soil erosion: Processes, prediction, measurement, and control*. New York: John Wiley & Sons.

Vandenbruwaene, W., Meire, P., & Temmerman, S. (2012). Formation and evolution of a tidal channel network within a constructed tidal marsh. *Geomorphology*, *151*, 114–125.

Vandenbruwaene, W., Temmerman, S., Bouma, T., Klaassen, P., De Vries, M., Callaghan, D., … Meire1, P. (2011). Flow interaction with dynamic vegetation patches: Implications for biogeomorphic evolution of a tidal landscape. *Journal of Geophysical Research: Earth Surface*, *116*(F01008), 1–13.

van der Wegen, M. (2013). Numerical modeling of the impact of sea level rise on tidal basin morphodynamics. *Journal of Geophysical Research: Earth Surface*, *118*(2), 447–460.

van der Wegen, M., Dastgheib, A., & Roelvink, J. (2010). Morphodynamic modeling of tidal channel evolution in comparison to empirical P-A relationship. *Coastal Engineering*, *57*(9), 827–837.

van der Wegen, M., & Roelvink, J. (2008). Long-term morphodynamic evolution of a tidal embayment using a two-dimensional, process-based model. *Journal of*

Geophysical Research: Oceans, *113*(C03016), 1–23.

van Maanen, B., Coco, G., Bryan, K. R., & Friedrichs, C. T. (2013). Modeling the morphodynamic response of tidal embayments to sea-level rise. *Ocean Dynamics*, *63*(11-12), 1249–1262.

van Oyen, T., Carniello, L., D'Alpaos, A., Temmerman, S., Troch, P., & Lanzoni, S. (2014). An approximate solution to the flow field on vegetated intertidal platforms: Applicability and limitations. *Journal of Geophysical Research: Earth Surface*, *119*(8), 1682–1703.

Venier, C., D'Alpaos, A., & Marani, M. (2014). Evaluation of sediment properties using wind and turbidity observations in the shallow tidal areas of the Venice Lagoon. *Journal of Geophysical Research: Earth Surface*, *119*(7), 1604–1616.

Wright, L., & Thom, B. (1977). Coastal depositional landforms: A morphodynamic approach. *Progress in Physical Geography*, *1*(3), 412–459.

Yallop, M. C., de Winder, B., Paterson, D. M., & Stal, L. J. (1994). Comparative structure, primary production and biogenic stabilisation of cohesive and non-cohesive marine sediments inhabited by microphytobenthos. *Estuarine Coastal Shelf Sciences*, *39*, 565-582.

Zedler, J. B., & Kercher, S. (2005). Wetland resources: Status, trends, ecosystem services, and restorability. *Annu. Rev. Environ. Resour.*, *30*, 39–74.

Zhao, K., Gong, Z., Xu, F., Zhou, Z., Zhang, C., Perillo, G. M. E., & Coco, G. (2019). The role of collapsed bank soil on tidal channel evolution: A process-based model involving bank collapse and sediment dynamics. *Water Resources Research*, *55*(11), 9051–9071.

Zhou, Z., Stefanon, L., Olabarrieta, M., D'Alpaos, A., Carniello, L., & Coco, G. (2014). Analysis of the drainage density of experimental and modelled tidal networks. *Earth Surface Dynamics*, *2*(1), 105–116.

Zhou, Z., Ye, Q., & Coco, G. (2016). A one-dimensional biomorphodynamic model of tidal flats: Sediment sorting, marsh distribution, and carbon accumulation under sea level rise. *Advances in Water Resources*, *93*, 288–302.